Grid convergence for numerical solutions of stochastic moment equations of groundwater flow

Chuan-An Xia[1], Alberto Guadagnini[* 2, 3], Bill X. Hu[* 1], Monica Riva[2, 3], Philippe Ackerer[2, 4]

[1] Institute of Groundwater and Earth Science, Jinan University, Guangzhou, China 510632.

[2] Dipartimento di Ingegneria Civile e Ambientale, Politecnico di Milano, Milan, Italy.

[3] Department of Hydrology and Atmospheric Sciences, The University of Arizona, Tucson, USA.

[4] Univ Strasbourg, CNRS, Lab Hydrol & Geochim Strasbourg, 1 Rue Blessig, F-67084 Strasbourg, France.

Submitted to

Stochastic Environmental Research and Risk Assessment

*Corresponding author: Alberto Guadagnini; Bill X. Hu

Tel:

Email: alberto.guadagnini@polimi.it; bill.x.hu@gmail.com

Abstract:

We provide qualitative and quantitative assessment of the results of a grid convergence study in terms of (*a*) the rate/order of convergence and (*b*) the Grid Convergence Index, GCI, associated with the numerical solutions of Moment Equations (MEs) of steady-state groundwater flow. The latter are approximated at second order (in terms of the standard deviation of the natural logarithm, *Y*, of hydraulic conductivity). We consider (*i*) the analytical solutions of Riva et al. (2001) for steady-state radial flow in a randomly heterogeneous conductivity field, which we take as references; and (*ii*) the numerical solutions of the MEs satisfied by the (ensemble) mean and (co)variance of hydraulic head and fluxes. Based on 45 numerical grids associated with differing degrees of discretization, we find a supra-linear rate of convergence for the mean and (co)variance of hydraulic head and for the variance of the transverse component of fluxes, the variance of radial fluxes being characterized by a sub-linear convergence rate. Our estimated values of GCI suggest that an accurate computation of mean and (co)variance of head and fluxes requires a space discretization comprising at least 8 grid elements per correlation length of *Y*, an even finer discretization being required for an accurate representation of the second-order component of mean heads.

Keywords: stochastic moment equations; groundwater flow; grid convergence index; Richardson extrapolation.

1. Introduction

Modeling of groundwater flow in natural aquifer systems is affected by a variety of sources of uncertainty. In this context, our incomplete knowledge of spatial distributions of hydrogeological attributes, such as hydraulic conductivity, inevitably propagates to results of numerical models. A convenient way to deal with such uncertainty is to conceptualize system attributes as random spatial fields, thus leading to a stochastic description of groundwater flow and/or transport.

In this context, a wide range of stochastic approaches are available including, e.g., techniques based on numerical Monte Carlo simulations and moment differential equations (or moment equations, MEs). Our study is focused on moment differential equations of fully saturated steady-state confined groundwater flow (see, e.g., Tartakovsky and Neuman, 1997; Zhang, 2002; Li and Tchelepi, 2003, 2004; Li et al., 2003; or Winter et al., 2003 for a review on moment differential equations for groundwater flow in highly heterogeneous porous media). The latter are deterministic equations rendering the (ensemble) moments of hydraulic head $h(\mathbf{x})$ and Darcy flux $\mathbf{q}(\mathbf{x})$ at location vector $\mathbf{x}$. Moment equations are obtained from the stochastic flow and mass conservation equations by integration in probability space. While the resulting system of MEs is almost never closed, closure approximations employed to make MEs workable are typically grounded on perturbation expansions (see also Section 2). Advantages of MEs-based approaches to groundwater flow as compared to numerical Monte Carlo (MC) simulations include the observation that

MEs provide insights on the nature of the solution which can hardly be achieved through a MC framework. Additionally, MC-based approaches rely on numerical solutions of the flow equation across a collection of many detailed realizations of hydraulic conductivity to capture the effects of heterogeneity. In some cases, this can lead to high computational costs, which can hamper the efficiency of MC-based analyses.

Moment differential equations of groundwater flow have been recently applied to field settings (Riva et al., 2009; Bianchi Janetti et al., 2010; Panzeri et al., 2015), to non-Gaussian fields (e.g., Hristopulos, 2006; Riva et al., 2017) and have been embedded in geostatistical inverse modeling approaches (Hernandez et al. 2003), stochastic pumping test interpretation (Neuman et al., 2004, 2007), or reactive solute transport (e.g., Hu et al., 2004). Most recent developments have allowed embedding stochastic MEs of transient groundwater flow in data assimilation/integration and parameter estimation approaches, e.g., via ensemble Kalman filter (Li and Tchelepi, 2006; Panzeri et al., 2013, 2015).

It can be argued that grids required to accurately represent the spatial distributions of inputs to MEs can be coarser than those associated with MC simulations, MEs being grounded on smoothed, ensemble mean parameters. Nevertheless, an assessment of the degree of approximation introduced by a given numerical grid employed to solve MEs is still lacking. In this context, it is noted that the full set of MEs (i.e., the equations governing the spatial distribution of ensemble mean or variance-covariance) for steady-state groundwater flow are characterized by the same mathematical format, while being associated with differing forcing terms (see also Section 2). As such, the nature of such forcing terms can play a main role in driving numerical grid convergence studies and results.

While a number of grid refinement analyses have been conducted on subsurface flow and transport settings (see, e.g., Slough et al., 1999; Weatherill et al., 2008; Graf and Degener, 2011), these have mainly been framed in a deterministic modeling framework. As such, they yield only limited insights about the dependencies of numerical grid size on the main geostatistical descriptors of aquifer heterogeneity. Leube et al. (2013) provided guidance about the selection of the spatial resolution of a numerical grid employed to solve groundwater flow in randomly heterogeneous reservoirs in a MC context. These authors apportion the computational complexity of numerical MC simulations according to spatial and temporal grid resolution, as well as the number of realizations to be considered in the collection employed to evaluate statistics (or quantiles) of interest. Recently, Maina et al. (2018) compared several numerical approaches to simulate breakthrough curves of solute concentrations measured during laboratory experiments performed on flow cells filled with various configurations of heterogeneous sands. Their results suggest that spatial discretization is significantly important to obtain accurate solutions in heterogeneous domains.

The two main objectives of our study are the assessment of the order of convergence, p, and the analysis of the results of systematic grid convergence studies for numerical solutions of steady-state groundwater flow MEs. Quantities of interest are the (ensemble) mean of hydraulic head, $h(\mathbf{x})$, and flux vector, $\mathbf{q}(\mathbf{x})$, as well as the corresponding spatial covariances. The qualities of the ensuing solutions are estimated through the Grid Convergence Index (GCI), which relies on a grid refinement error estimator grounded on the generalized Richardson extrapolation (Richardson, 1910; Richardson and Gaunt, 1927). As a reference against which solution accuracies of MEs are evaluated, we leverage on the analytical expressions developed by Riva et al. (2001) for leading statistical moments of $h(\mathbf{x})$ and $\mathbf{q}(\mathbf{x})$ under steady-state convergent flow to a well operating in a bounded, randomly heterogeneous reservoir.

This study is organized as follows. Section 2 illustrates the MEs we analyze. Section 3 presents the details of the convergence study for the MEs. Sections 4 and 5 illustrate the set of numerical analyses and associated results, respectively. Section 6 is devoted to our main conclusions.

2. Theoretical Background for Moment Equations of steady-state groundwater flow

Consider steady-state groundwater flow described by:

$$\left.\begin{aligned} -\nabla_x \cdot \mathbf{q}(\mathbf{x}) + f(\mathbf{x}) &= 0 \\ \mathbf{q}(\mathbf{x}) &= -K(\mathbf{x}) h(\mathbf{x}) \end{aligned}\right\} \tag{1}$$

subject to boundary conditions

$$h(\mathbf{x}) = H(\mathbf{x}) \qquad \mathbf{x} \in \Gamma_D \tag{2}$$

$$[-\mathbf{q}(\mathbf{x})]\cdot\mathbf{n}(\mathbf{x}) = Q(\mathbf{x}) \qquad \mathbf{x}\in\Gamma_N \tag{3}$$

Here, $\mathbf{x}$ is the vector of spatial coordinates within domain Ω; $\nabla_x \cdot$ is the spatial gradient operator; $f(\mathbf{x})$ is a (generally random) forcing term; $K(\mathbf{x})$ is hydraulic conductivity; $\mathbf{n}(\mathbf{x})$ is the unit vector normal to Neumann boundary Γ_N; $Q(\mathbf{x})$ is the (typically random) flux along Γ_N; $H(\mathbf{x})$ is a random head along Dirichlet boundary Γ_D.

For simplicity, we consider $f(\mathbf{x})$, $H(\mathbf{x})$ and $Q(\mathbf{x})$ as deterministic in our analyses. Hydraulic conductivity $K(\mathbf{x})$ is taken to be a random spatial field, its fluctuation about the (ensemble) mean $\langle K(\mathbf{x})\rangle$ being expressed as $K'(\mathbf{x}) = K(\mathbf{x}) - \langle K(\mathbf{x})\rangle$. We introduce $h'(\mathbf{x}) = h(\mathbf{x}) - \langle h(\mathbf{x})\rangle$ as the random fluctuation of hydraulic head, $h(\mathbf{x})$, about (ensemble) mean, $\langle h(\mathbf{x})\rangle$. One can then recast (1)-(3) as

$$\nabla_x \cdot [\langle K(\mathbf{x})\rangle \nabla_x \langle h(\mathbf{x})\rangle + \langle K(\mathbf{x})\rangle \nabla_x h'(\mathbf{x}) + K'(\mathbf{x})\nabla_x \langle h(\mathbf{x})\rangle + K'(\mathbf{x})\nabla_x h'(\mathbf{x})] + f(\mathbf{x}) = 0 \tag{4}$$

subject to boundary conditions

$$\langle h(\mathbf{x})\rangle + h'(\mathbf{x}) = H(\mathbf{x}) \qquad \mathbf{x}\in\Gamma_D \tag{5}$$

$$\begin{bmatrix} \langle K(\mathbf{x})\rangle \nabla_x \langle h(\mathbf{x})\rangle + \langle K(\mathbf{x})\rangle \nabla_x h'(\mathbf{x}) \\ + K'(\mathbf{x})\nabla_x \langle h(\mathbf{x})\rangle + K'(\mathbf{x})\nabla_x h'(\mathbf{x}) \end{bmatrix} \cdot \mathbf{n}(\mathbf{x}) = Q(\mathbf{x}) \qquad \mathbf{x}\in\Gamma_N \tag{6}$$

Taking ensemble averages of (4)-(6) yields exact equations satisfied by $\langle h(\mathbf{x})\rangle$ (see, e.g., Guadagnini and Neuman, 1999a; Zhang, 2002). Following these authors, it is then possible to obtain exact equations satisfied by the covariance of heads and/or the cross-covariance between conductivity and heads, as well as expressions for the covariance tensor of flux. A strategy to solve these (deterministic) MEs relies on expanding all moments appearing in them in terms of a small parameter σ_Y, representing the standard deviation of the natural logarithm of hydraulic conductivity, i.e., $Y(\mathbf{x}) = \ln K(\mathbf{x})$. We then obtain a set of recursive approximations of the otherwise exact MEs which we can solve up to a given order (expressed in terms of powers of σ_Y). Each equation rendering a given order of approximation of a moment of interest is then local in space. In the following sections, we summarize the main formulations associated with the equations satisfied by low order approximations of ensemble mean and covariance of hydraulic heads and fluxes. Further details about the complete derivation of such equations are included, e.g., in Guadagnini and Neuman (1999a) and Zhang (2002).

2.1 Zero-order mean head and flux

The equation for the zero-order mean head $\left\langle h^{(0)}(\mathbf{x})\right\rangle$ is expressed as:

$$\nabla_x \cdot \left[K_G(\mathbf{x}) \nabla_x \left\langle h^{(0)}(\mathbf{x})\right\rangle \right] + f(\mathbf{x}) = 0 \qquad (7)$$

subject to boundary conditions:

$$\left\langle h^{(0)}(\mathbf{x})\right\rangle = H(\mathbf{x}) \qquad \mathbf{x} \in \Gamma_D \qquad (8)$$

$$\left[-\left\langle \mathbf{q}^{(0)}(\mathbf{x})\right\rangle \right] \cdot \mathbf{n}(\mathbf{x}) = Q(\mathbf{x}) \qquad \mathbf{x} \in \Gamma_N \qquad (9)$$

Here and in the following, superscript (i) identifies terms that are strictly of order i (in terms of powers of σ_Y), $K_G(\mathbf{x}) = e^{\langle Y(\mathbf{x})\rangle}$ is the geometric mean of $K(\mathbf{x})$, and $\left\langle \mathbf{q}^{(0)}(\mathbf{x})\right\rangle = -K_G(\mathbf{x}) \nabla_x \left\langle h^{(0)}(\mathbf{x})\right\rangle$ is the zero-order mean flux vector.

2.2 Second-order cross covariance between head and conductivity

Multiplying Eqs. (4-6) by $K'(\mathbf{y})$, taking expectation and expanding the resulting equations yield the following equations for the second-order approximation of the cross covariance of head and conductivity, $u^{(2)}(\mathbf{y},\mathbf{x})=\left\langle K^{'}(\mathbf{y})h^{'}(\mathbf{x})\right\rangle^{(2)}$:

$$\nabla_x\cdot\left[K_G(\mathbf{x})\nabla_x u^{(2)}(\mathbf{y},\mathbf{x})-K_G(\mathbf{y})C_Y(\mathbf{x},\mathbf{y})\left\langle \mathbf{q}^{(0)}(\mathbf{x})\right\rangle\right]=0 \qquad (10)$$

subject to boundary conditions:

$$u^{(2)}(\mathbf{y},\mathbf{x})=0 \qquad \mathbf{x}\in\Gamma_D \qquad (11)$$

$$\left[K_G(\mathbf{x})\nabla_x u^{(2)}(\mathbf{y},\mathbf{x})-K_G(\mathbf{y})C_Y(\mathbf{x},\mathbf{y})\left\langle \mathbf{q}^{(0)}(\mathbf{x})\right\rangle\right]\cdot\mathbf{n}(\mathbf{x})=0 \qquad \mathbf{x}\in\Gamma_N \qquad (12)$$

Here, $C_Y(\mathbf{x},\mathbf{y})=\left\langle Y^{'}(\mathbf{x})Y^{'}(\mathbf{y})\right\rangle$ is the covariance of Y between locations $\mathbf{x}$ and $\mathbf{y}$ in the domain.

2.3 Second-order head covariance

Multiplying Eqs. (4-6) by head fluctuation $h^{'}(\mathbf{y})$, taking expectation and expanding the resulting equations yield the following equations for the second-order head covariance, $C_h^{(2)}(\mathbf{y},\mathbf{x})=\left\langle h^{'}(\mathbf{y})h^{'}(\mathbf{x})\right\rangle^{(2)}$:

$$\nabla_x\cdot\left[K_G(\mathbf{x})\nabla_x C_h^{(2)}(\mathbf{y},\mathbf{x})+u^{(2)}(\mathbf{x},\mathbf{y})\nabla_x\left\langle h^{(0)}(\mathbf{x})\right\rangle\right]=0 \qquad (13)$$

subject to boundary conditions:

$$C_h^{(2)}(\mathbf{y},\mathbf{x})=0 \qquad \mathbf{x}\in\Gamma_D \qquad (14)$$

$$\left[K_G(\mathbf{x})\nabla_x C_h^{(2)}(\mathbf{y},\mathbf{x})+u^{(2)}(\mathbf{x},\mathbf{y})\nabla_x\left\langle h^{(0)}(\mathbf{x})\right\rangle\right]\cdot\mathbf{n}(\mathbf{x})=0 \qquad \mathbf{x}\in\Gamma_N \qquad (15)$$

where $u^{(2)}(\mathbf{x},\mathbf{y})=\left\langle K^{'}(\mathbf{x})h^{'}(\mathbf{y})\right\rangle^{(2)}$ is given by Eqs. (10)-(12).

2.4 Second-order mean head and flux

The equation satisfied by the second-order mean head $\left\langle h^{(2)}(\mathbf{x})\right\rangle$ is:

$$\nabla_x\cdot\left[K_G(\mathbf{x})\left[\nabla_x\left\langle h^{(2)}(\mathbf{x})\right\rangle+\frac{\sigma_Y^2}{2}\nabla_x\left\langle h^{(0)}(\mathbf{x})\right\rangle\right]-\mathbf{r}^{(2)}(\mathbf{x})\right]=0 \qquad (16)$$

subject to boundary conditions:

$$\left\langle h^{(2)}(\mathbf{x})\right\rangle = 0 \qquad \mathbf{x} \in \Gamma_D \tag{17}$$

$$\left[-\left\langle \mathbf{q}^{(2)}(\mathbf{x})\right\rangle\right]\cdot \mathbf{n}(\mathbf{x}) = 0 \qquad \mathbf{x} \in \Gamma_N \tag{18}$$

Here, $\left\langle \mathbf{q}^{(2)}(\mathbf{x})\right\rangle = -K_G(\mathbf{x})\left(\nabla_x \left\langle h^{(2)}(\mathbf{x})\right\rangle + \frac{\sigma_Y^2}{2}\nabla_x \left\langle h^{(0)}(\mathbf{x})\right\rangle\right) + \mathbf{r}^{(2)}(\mathbf{x})$ and $\mathbf{r}^{(2)}(\mathbf{x}) = -\nabla_x u^{(2)}(\mathbf{x},\mathbf{x})$ are a second-order mean flux vector and the residual flux, respectively.

We evaluate the second-order residual flux by taking the limit for $\mathbf{y} \to \mathbf{x}$ of the negative of $\nabla_x u^{(2)}(\mathbf{y},\mathbf{x})$, as:

$$\mathbf{r}^{(2)}(\mathbf{x}) = \lim_{y \to x}\left[-\nabla_x u^{(2)}(\mathbf{y},\mathbf{x})\right] \tag{19}$$

where $u^{(2)}(\mathbf{y},\mathbf{x})$ is given by Eqs. (10)-(12).

We note that Guadagnini and Neuman (1999a, b) relied on a strategy based on a Green's function approach to compute the second-order residual flux, which is expressed as $\mathbf{r}^{(2)}(\mathbf{x}) = \int_\Omega K_G(\mathbf{x})K_G(\mathbf{y})\left\langle Y'(\mathbf{x})Y'(\mathbf{y})\right\rangle \nabla_x \nabla_y^{\mathrm{T}} \left\langle G^{(0)}(\mathbf{y},\mathbf{x})\right\rangle \nabla_y \left\langle h^{(0)}(\mathbf{y})\right\rangle dy$, subscript T representing transpose, and $\left\langle G^{(0)}(\mathbf{y},\mathbf{x})\right\rangle$ being the zero-order mean Green's function associated with the flow problem (see Guadagnini and Neuman, 1999a, for details). This approach has then been employed in subsequent studies (e.g., Ye et al., 2004). It is apparent that the main computation cost associated with this scheme stems from the need to solve the equation satisfied by $\left\langle G^{(0)}(\mathbf{y},\mathbf{x})\right\rangle$ for a number of times corresponding to the number of computational nodes in domain Ω, evaluating the corresponding partial derivatives, and then performing integration over Ω. Computational times associated with this approach are then exacerbated when considering transient flow (see Ye et al., 2004). All of these aspects constitute a limitation when considering inverse modeling for geostatistical aquifer characterization based on Moment Equations. This is the key motivation for which we resort here to Eqs. (10)-(12), and (19) to evaluate $\mathbf{r}^{(2)}(\mathbf{x})$ at a much reduced computational effort.

2.5 Second-order tensor of flux covariance

The second-order flux covariance tensor $\mathbf{C}_q^{(2)}(\mathbf{x},\mathbf{y}) = \langle \mathbf{q}'(\mathbf{x})\, \mathbf{q}'^{\mathrm{T}}(\mathbf{y}) \rangle^{(2)}$ satisfies the following equation:

$$\begin{aligned}\mathbf{C}_q^{(2)}(\mathbf{x},\mathbf{y}) = K_G(\mathbf{x}) K_G(\mathbf{y}) [&\nabla_x \nabla_y^{\mathrm{T}} C_h^{(2)}(\mathbf{x},\mathbf{y}) \\ &+ \nabla_x \langle h^{(0)}(\mathbf{x}) \rangle \nabla_y^{\mathrm{T}} \langle h^{(0)}(\mathbf{y}) \rangle C_Y(\mathbf{x},\mathbf{y}) \\ &+ \nabla_x \langle h^{(0)}(\mathbf{x}) \rangle \nabla_y^{\mathrm{T}} u^{(2)}(\mathbf{x},\mathbf{y}) \\ &+ \nabla_x u^{(2)}(\mathbf{y},\mathbf{x}) \nabla_y^{\mathrm{T}} \langle h^{(0)}(\mathbf{y}) \rangle]\end{aligned} \qquad (20)$$

Solutions of Eqs. (7)-(15) constitute the inputs to (20).

2.6 Numerical approach

Evaluation of the statistical moments introduced above is performed in a sequential way. We start by computing the zero-order mean head, $\langle h^{(0)} \rangle$, through Eqs. (7-9). Note that all other quantities of interest depend on $\langle h^{(0)} \rangle$. The zero-order mean flux, $\langle \mathbf{q}^{(0)} \rangle$, is obtained through Darcy's law using the derivatives of the numerical approximation of $\langle h^{(0)} \rangle$. Neither $\langle h^{(0)} \rangle$ nor $\langle \mathbf{q}^{(0)} \rangle$ depend on the covariance of *Y*.

The second-order cross covariance between head and conductivity, $u^{(2)}(\mathbf{y},\mathbf{x})$, is obtained by solving (10-12) and depends on the covariance of *Y* and on $\langle \mathbf{q}^{(0)} \rangle$. Quantities such as $\langle h^{(2)} \rangle$, $\langle \mathbf{q}^{(2)} \rangle$, and $C_h^{(2)}$ depend strongly on $u^{(2)}$. The latter must then be computed accurately and grid discretization should be fine enough to properly describe the contribution of the covariance function of Y to $u^{(2)}$. In other words, if the distance between two adjacent nodes on the computational grid is larger than the correlation length of Y, the covariance function in Eq. (10) between such nodes will tend to vanish. This would in turn lead to a poor approximation of $u^{(2)}$, thus impacting on the quality of the results associated with all quantities that depend on $u^{(2)}$.

From a numerical point of view, Eqs. (7), (10), (13), and (16) share the same format, i.e., all of them can be cast in terms of the divergence of the gradient of a given moment multiplied by K_G, under the action of a sink/source term. Thus, their discretization leads to systems of equations where the coefficients of the unknown quantities are identical, the right-hand side (i.e., the force term) depending on the moment to be solved. In this context, one can resort to a direct solver, which allows for the transformation (factorization) of the matrix containing the coefficients of the system of equations. This transformation is performed only once and the transformed matrix enables one to solve the system of equations in a very efficient way, because only the right-hand side needs to be updated depending on the moment of interest. The MEs are here solved by linear Galerkin finite elements.

3. Grid Convergence for Moment Equations

We take the analytical solutions of moments of steady-state flow to a well of Riva et al. (2001) as the exact results, F_{exact}, against which the quality of numerical solutions of the MEs illustrated in Section 2 is assessed. We focus on requirements for grid convergence of the equations satisfied by $\langle h^{(0)}(\mathbf{x})\rangle$, $u^{(2)}(\mathbf{y},\mathbf{x})$, $C_h^{(2)}(\mathbf{y},\mathbf{x})$ and $\langle h^{(2)}(\mathbf{x})\rangle$. It is remarked that while the equations satisfied by these quantities are characterized by the same mathematical format, they are associated with differing forcing terms. The latter feature can influence the rate p of grid convergence which we examine in this study.

A grid convergence/refinement study is a procedure that enables us to explore the effect of a given grid discretization level on the accuracy of the numerical solution of a target mathematical model. We estimate the orders p of grid convergence of the solutions of equations illustrated in Section 2 by the two procedures described in the following.

3.1 Rate of Convergence

We start by defining the quantity:

$$E(\vartheta) = F(\vartheta) - F_{exact} = C\vartheta^{p} + O\left(p\right) \tag{21}$$

where ϑ is a metric representing grid spacing; and $E(\vartheta)$ is the error between the numerical solution $F(\vartheta)$ related to grid spacing ϑ and F_{exact} (i.e., the exact solution), $O\left(p\right)$ representing higher order terms. One can then estimate C and p in (21) from a linear regression on results obtained on multiple grids, according to:

$$\ln E(\vartheta) \approx \ln C + p\ln\vartheta \tag{22}$$

We follow Vassberg and Jameson (2010) and take $\vartheta = \sqrt{1/N}$, N being the number of nodes (i.e. number of unknowns) of a given computational grid. The regression result typically depends on the number of grids used to perform the analysis. As we state in Section 4, our study relies on a total of 15 families of unstructured grids. Each family comprises a coarse, an intermediate and a fine grid, constructed according a constant/uniform grid refinement ratio. We then obtain a total of 3 values of ϑ for each grid family. As such, we can perform regression to estimate C and p on the basis of 45 values of $E(\vartheta)$ for target moment and location in the domain. We do so for the set of (statistical) moments of interest (see Section 4).

3.2 Grid Convergence Index

We note that, in general, F_{exact} is unknown, this being a key reason underpinning grid convergence studies. We consider three grid refinement levels for each of the 15 grid families mentioned in Section 3.1 (see also Section 4), i.e., a coarse, an intermediate, and a fine level (hereafter termed ϑ_c, ϑ_m, and ϑ_f, respectively) and evaluate the corresponding (numerical) solutions $F(\vartheta_i)$ = F_i ($i = c$, m, or f). One can then estimate p from (21) as:

$$p \approx \ln\left(\frac{F_c - F_m}{F_m - F_f}\right) / \ln(\omega) \tag{23}$$

where $\omega = \vartheta_c / \vartheta_m = \vartheta_m / \vartheta_f$ is a (constant) grid refinement ratio. High values of p correspond to high convergence rates. We can calculate 15 values of p in our analyses, one for each grid family we construct. We can also evaluate the quality of the convergence, based on the indicator (Stern et al., 2001):

$$\mu = \varepsilon_{m,f} / \varepsilon_{c,m}; \quad \text{with } \varepsilon_{c,m} = F_c - F_m; \text{ and } \varepsilon_{m,f} = F_m - F_f \tag{24}$$

where one can distinguish among monotonic ($0<\mu<1$) or oscillatory ($\mu<0$) convergence; and divergence ($\mu>1$). It is worth noting that values of $\mu \approx 1$ indicate that p is close to zero (see (23)) which means that the numerical solution is not sensitive to the grid size.

We then calculate a Grid Convergence Index (GCI) for each grid family. This index rests on the theory of the generalized Richardson extrapolation and provides a measure of grid convergence as well as an error band for the grid convergence of the solution (Roache, 1994) and is defined as

$$\mathrm{GCI}_{k,s} = S_F \frac{|F_k - F_s|}{|F_s|\left(\omega^p - 1\right)} \times 100\% \quad (25)$$

Here, $\mathrm{GCI}_{k,s}$ is the grid convergence index corresponding to numerical solutions F_k and F_s; and S_F is a safety factor, which is typically set to 1.25 when three-grid levels are employed.

4 Numerical analyses for radial flow configuration

4.1 Numerical settings

Consistent with the setting of Riva et al. (2001), we perform our grid convergence study on a two-dimensional domain formed by a circle of radius L (Figure 1a) and centered at the origin of a selected coordinate system. Domain discretization is implemented through an unstructured triangular mesh. Boundary conditions are of Dirichlet type and are considered as uniform and known (i.e., head is set to 0). A zero-radius well with a deterministic unit pumping rate is operating at the domain center. Hydraulic conductivity $K(\mathbf{x})$ is considered as a (second-order stationary) spatial random field characterized by a Gaussian covariance function defined by:

$$C_Y(\delta) = \sigma_Y^2 \exp\left[-\frac{\pi}{4}\frac{\delta^2}{\lambda^2}\right] \tag{26}$$

where δ separation distance (lag) between two locations, σ_Y^2 is the variance of $Y(\mathbf{x})$ and λ the (isotropic) correlation scale.

The accuracies of the numerical simulations are analyzed by comparison against the analytical solutions provided by Riva et al. (2001). These authors derived analytical solutions for second-order (statistical) moments of head and flux in terms of four-dimensional integrals. These are evaluated at given locations in the domain by Gaussian quadrature relying on 500 Gauss points. The moments of interest, i.e., $\langle h^{(0)} \rangle$, $\langle h^{(2)} \rangle$, $\sigma_h^{2(2)}$ and the components of (second-order) flux variance tensor, i.e., $\sigma_{qr}^{2(2)}$, $\sigma_{q\theta}^{2(2)}$, and $\sigma_{qr\theta}^{2(2)} = \sigma_{q\theta r}^{2(2)}$, are evaluated at $N_r = 100$ (dimensionless) values of $\xi = r / L$ (*r* being distance from the well). These moments do not depend on the angular coordinate due to symmetry. The selected 100 values of ξ are distributed according to a geometric progression, i.e., following an arithmetic progression of the log-transformed values of ξ, with ln(0.01) ≤ ξ ≤ ln(0.99) and considering a constant increment of $\frac{1}{99} \times \ln 99$.

Since we rely on an unstructured mesh, we cannot take advantage of symmetry. The numerical solutions are computed at the above indicated N_r locations and at a set of $N_\theta = 100$ angular coordinates (ranging according to $0 \le \theta \le 99\pi / 50$, with a regular increment of $\pi / 50$) for each radial distance. The ensuing $N_r \times N_\theta$

reference locations are depicted in Figure 1a, the spatial arrangement of ξ values being depicted in Figure 1b for a given θ.

The second-order head covariance $C_h^{(2)}$ between locations (ξ, θ) and ($\xi^{'}, \theta^{'}$) is symmetric with respect to either $\left(\xi - \xi^{'}\right)$ (when $\theta - \theta^{'} = 0$) or $\left(\theta - \theta^{'}\right)$ (when $\xi - \xi^{'} = 0$). We consider three given $\xi^{'}$ values (i.e., $\xi^{'}$ = 0.2, 0.5, and 0.8) and define two sets of reference locations at which we compute head covariances. The first set corresponds to three locations having the same angular coordinate and differing radial coordinates. A second set is formed by three locations with the same radial coordinate and differing θ. In the following, we denote by $C_h^{(2)}\left(\xi, \xi_1^{'}\right)$, $C_h^{(2)}\left(\xi, \xi_2^{'}\right)$ and $C_h^{(2)}\left(\xi, \xi_3^{'}\right)$ the solutions of the first set of reference points and by $C_h^{(2)}\left(\theta, \xi_1^{'}\right)$, $C_h^{(2)}\left(\theta, \xi_2^{'}\right)$ and $C_h^{(2)}\left(\theta, \xi_3^{'}\right)$ the corresponding solutions associated with the second set of reference points.

The analytical solution for a given distance ξ is compared to the 100 numerical solutions obtained at the same distance to the well and corresponding to differing values of θ. Numerical solutions are first calculated at the nodes of the triangular mesh and then projected (through linear interpolation) onto the closest reference locations where analytical solutions are evaluated.

Solutions for means and variances are stored in a $N_r \times N_\theta$ matrix $\mathbf{S}$, whose entry S_{ij} is the numerical solution at radial coordinate ξ_i and angular coordinate θ_j. The size of the matrix associated with corresponding solutions for head covariances is $N_r \times N_r$ or $N_\theta \times N_\theta$ for the two sets of reference points above illustrated, respectively. Entry S_{ij} of $\mathbf{S}$ is then the numerical solution of head covariance at radial (ξ_i and ξ_j) or angular (θ_i and θ_j) coordinates, for the first and second set of reference points, respectively.

Numerical errors are estimated through the root mean square error for a given ξ_i, i.e.,

$$E_r^i = \sqrt{\frac{1}{N_\theta}\sum_{j=1}^{N_\theta}\left(S_{ij} - S_i^a\right)^2} \tag{27}$$

and by way of the global quantity

$$E_r = \frac{1}{N_r}\sum_{i=1}^{N_r} E_r^i \tag{28}$$

S_{ij} and S_i^a being the numerical and the analytical solutions, respectively.

4.2 Domain discretization and test cases

We conduct our grid convergence study by relying on 15 grid families. The 15 initial triangular meshes, each associated with a given element size (expressed as $\zeta = \lambda / \Delta x$ in Table 1, Δx being the grid size) and termed as coarse meshes, are generated with the public domain mesh generator Gmsh (Geuzaine and Remacle, 2009). These initial meshes are then refined by dividing each triangle into 4 regular sub-triangles to obtain the medium meshes (Table 1). The latter are further refined (using the same procedure) to obtain the fine meshes. MEs are then solved on the collection of 45 different unstructured meshes listed in Table 1. Numerical simulations are hereafter termed as $TC_{i,j}$ (subscripts i = 1, 2, …, 15, and j = c, m, and f representing the grid family and the level of refinement, respectively). Note that the initial nodes employed during the generation of the coarse mesh in the i^{th} family are then shared by the corresponding medium and fine meshes. Grid refinement also includes additional nodes, specifically employed to describe the domain boundary and generated as shown in Figure 2.

Numerical solutions of the various (statistical) moments of interest are computed for a combination of values of K_G and σ_Y^2, and for $\kappa = L/\lambda$ = 1, and 3.

5. Results and Discussion

5.1 Qualitative comparisons against analytical solutions

Figure 3 juxtaposes the numerical and analytical solutions for the zero- ($\langle h^{(0)} \rangle$) and second- ($\langle h^{(2)} \rangle$) order mean heads, as well as second-order head variance ($\sigma_h^{2(2)}$) for $TC_{1,c}$ and $TC_{15,f}$, respectively associated with the coarsest and finest grids considered. Corresponding comparisons for the components of second-order flux variance tensors are depicted in Figure 4. Figures 5 and 6 depict the results obtained for the two sets of head covariances corresponding to the reference points indicated in Section 4.1. As expected, numerical errors for the coarse mesh are visibly significant at locations characterized by marked spatial gradients of the solution (i.e., close to the well), the quality of the numerical results significantly increasing with the level of discretization. Values of the cross component $\sigma_{qr\theta}^{2(2)}$ are very small and fluctuating around their analytical counterpart, which is equal to zero (Riva et al., 2001). It has to be noticed that errors are also associated with the required (linear) interpolations of the numerical solutions. This is especially critical close to the well where heads tend to vary in a way which is akin to a logarithmic trend. The Dirichlet boundary contributes to stabilize the numerical solution far from the well, independent of the discretization. The seemingly periodic fluctuations appearing for the head covariance associated with $TC_{1,c}$ (Fig. 6) are likely due to the combined effects of the interpolation and of the spatial structure of the grid.

5.2 Grid convergence

Figure 7 depicts $\ln E_r$ (28) versus the total number of nodes associated with each of the numerical grids employed, as rendered by $\ln(\vartheta) = -0.5\ln(N)$. Straight (solid or dashed) lines are the results of (least square) linear regressions on numerical results. According to Eq. (21), the slopes of these regression lines correspond to estimates of the convergence orders (*p*) of the numerical solutions. The values of *p* and of the determination coefficients (R^2) of the regressions are listed in Table 2.

Results included in Figure 7b and Table 2 show that numerical solutions for $C_h^{(2)}(\xi, \xi_1^{'})$, $C_h^{(2)}(\xi, \xi_2^{'})$ and $C_h^{(2)}(\xi, \xi_3^{'})$ are associated with virtually the same value of *p*, a similar observation holding also for the second set of head covariance solutions. With reference to the latter, we note that their associated convergence orders are higher than those we find for any of the (statistical) moments considered. This result is partially attributed to the observation that numerical solutions for $C_h^{(2)}(\theta, \xi_1^{'})$, $C_h^{(2)}(\theta, \xi_2^{'})$ and $C_h^{(2)}(\theta, \xi_3^{'})$ are evaluated at positions apart from the pumping well (see the red plus symbols in Figure 1) and, as such, do not include the zone close to the pumping location where errors are highest. While the rate of convergence is supra-linear for the mean and (co)variance of hydraulic head and for the variance of the transverse component of fluxes, it is sub-linear for the variance of the radial component of fluxes.

Quantification of grid convergence order across the whole domain in the absence of a reference analytical solution (as is the case in a variety of flow scenarios in natural heterogeneous aquifers) can be assessed through Eq. (23) at nodes where the numerical solutions are characterized by monotonic convergence conditions (i.e., $0 < \mu < 1$; see Eq. (24)). In our study, we start by analyzing:

$$\alpha_i = N_i^{*mc} / N_i^{*} \times 100\% \qquad \text{with } i = 1, 2, \ldots, 15 \qquad (29)$$

Here, subscript i denotes the grid family; α_i is the percentage of grid nodes where monotonic convergence is attained for a given statistical moment of interest; N_i^{*mc} and N_i^{*} are the number of nodes associated with monotonic convergence condition and the initial number of nodes (i.e., the number of nodes in common to the coarse, medium and fine meshes), respectively. The dependence of α_i on the grid family for the various moments considered is depicted in Figure 8a. These results indicate that values of α_i for $\langle h^{(2)} \rangle$ are always close to 100%, while fluctuating around 90% for $\langle h^{(0)} \rangle$, $\sigma_h^{2(2)}$ and $C_{h\dagger}^{(2)}$ (the latter quantity is the head covariance solution at the reference point corresponding to coordinates (ξ, θ) ≡ (0.5, 0)). Figure 8b complements these results by depicting the values of $\overline{p}$ computed as averages of the corresponding values of p calculated through Eq. (23) at the fraction of nodes depicted in Figure 8a. These results reveal that similar average values of p, i.e., 1.6 ≤ $\overline{p}$ ≤ 1.9, are obtained for $\langle h^{(0)} \rangle$, $\langle h^{(2)} \rangle$, $\sigma_h^{2(2)}$ and $C_{h\,\dagger}^{(2)}$. These values are consistent with those listed in Table 2.

A global appraisal of the grid convergence index $\mathrm{GCI}_{c,m}$ (as calculated considering the coarse (c) and medium (m) mesh) for the whole domain can be obtained as the average of the nodal values of (25) computed at the N_i^{*mc} grid nodes. The dependence on the grid family of values of average $\mathrm{GCI}_{c,m}$ (denoted as $\overline{\mathrm{GCI}}_{c,m}$) are depicted in Figure 8c. It is noted that values of $\overline{\mathrm{GCI}}_{c,m}$ decrease with increasing $\zeta = \lambda / \Delta x$ (i.e., with decreasing grid size with respect to the correlation scale of Y) and converge to zero for all statistical moments. This finding implies that numerical convergence is attained, or, in other words, that a further mesh refinement does not lead to an improvement of the quality of the numerical results. As expected, we note that values of $\overline{\mathrm{GCI}}_{c,m}$ for the second-order components of the statistical moments analyzed generally display lower convergence rates as compared to $\langle h^{(0)} \rangle$. A significantly fine grid (in terms of number of grid nodes per correlation scale) is required to obtain accurate results for the second-order mean head, as compared to $\langle h^{(0)} \rangle$. Similar grid convergence behavior is observed for both L / λ = 1 and 3 (see the inset in Fig. 8c). On the basis of these results and Table 2, we note that grid convergence is achieved for $\lambda / \Delta x$ ≥ 8 for all statistical quantities except for the second-order mean head $\langle h^{(2)} \rangle$ that attains grid convergence for $\lambda / \Delta x$ ≥ 14 (for example, when considering $\langle h^{(2)} \rangle$ one can note that $\overline{\mathrm{GCI}}_{c,m}$ < 0.5% when $\lambda / \Delta x$

= 16).

5.3 Dependence of numerical errors on the mean and variance of log-conductivities

Here, we investigate the dependence on $\langle Y \rangle$ and σ_Y^2 of the errors associated with the numerical solutions of the MEs. We do so by considering two settings, respectively corresponding to (*i*) $\langle Y \rangle$ = – 2.3, – 0.7, 1.6, and 2.3 (corresponding to K_G = 0.1, 0.5, 5 and 10, in arbitrary consistent units) with σ_Y^2 = 1.0; and (*ii*) σ_Y^2 = 2, 4, 6 and 8 with $\langle Y \rangle$ = 0.0 (i.e., K_G = 1.0). We keep $\kappa = L / \lambda = 1$ in both settings.

Figures 9 and 10 depict the dependence of E_r (28) on $\langle Y \rangle$ and ϑ for the statistical moments considered. The error is significant for coarse meshes and low values of $\langle Y \rangle$ for all moments of head considered. Because boundary conditions and well pumping rate are (deterministically) prescribed, low values of $\langle Y \rangle$ give rise to marked head gradients and the linear interpolation employed tends to be ineffective. Errors associated with second-order flux variances appear to be insensitive to $\langle Y \rangle$. The pattern of errors associated with head covariances is similar to the one observed for the mean and variance (compare Figures 9 and 10), the errors decreasing with the distance from the well.

Figures 11 and 12 depict the dependence of E_r (28) on σ_Y^2 and ϑ for the statistical moments considered, with the exception of $\langle h^{(0)} \rangle$, which is independent of σ_Y^2 (see Eq. (7)). One can see that E_r generally increases with σ_Y^2 and ϑ. The impact of σ_Y^2 is consistent with the formats of the moment equations (see Eqs.

(10), (13), (16) and (20)) where σ_Y^2 appears as a multiplicative factor, thus potentially amplifying computational errors. For example, the head gradient in Eq. (10) is multiplied by σ_Y^2, thus amplifying (for $\sigma_Y^2 > 1$) the error due to the head gradient evaluation.

6. Conclusions

Values of grid convergence orders, *p*, of numerical solutions of moment equations (MEs) of steady-state groundwater flow are quantified. As test case, we consider convergent flow to a well taking place in a bounded randomly heterogeneous two-dimensional system and ground our results on comparisons between numerical solutions of MEs associated with multiple families of grids and the analytical solutions presented by Riva et al. (2001).

Our study leads to the following major conclusions.

1. The rate of convergence is (*a*) supra-linear for the mean and (co)variance of hydraulic head and for the variance of the transverse component of fluxes, and (*b*) sub-linear for the variance of the radial component of fluxes. Approximated values of average rate of convergence obtained by Eq. (23), relying on the use of numerical solutions of MEs associated with increasingly refined grids are consistent with their counterparts based on Eq. (22) and obtained as a linear regression on the errors between numerical and (reference) analytical solutions. Our results on grid convergence yield a pragmatic estimate of the accuracy improvement associated with the

evaluation of a given target statistical moment of groundwater flow with respect to grid refinement. As shown in Table 2, grid convergence rate depends on the given statistical moment, being a critical element in the evaluation of the variance of the radial component of flux while denoting the fastest achievement of a desired accuracy level for hydraulic head covariances. These findings can assist modelers to optimally refine numerical grids to achieve the highest accuracy associated with the desired prediction goal depending on the available computational resources.

2. The grid convergence index $\mathrm{GCI}_{c,m}$ (see Eq. (25)) associated with all of the statistical moments considered is shown to converge to zero with increased grid refinement. Our results suggest that employing a grid spacing $\Delta x \leq \lambda/8$ yields accurate approximations of all moments considered, an enhanced grid refinement (i.e., $\Delta x/\lambda \leq 1/14$) being required to attain grid convergence only for the second-order mean head.
3. Variations of log conductivity mean, K_G, and variance, σ_Y^2, show no appreciable impact on the percentage of nodes where uniform convergence is attained, rate of convergence, or the value of $\mathrm{GCI}_{c,m}$. In addition, decreasing K_G can yield increased solution errors for all computed statistical moments, with the exception of the components of second-order flux variance. Increasing σ_Y^2 can lead to enhanced solution errors for all of the second-order statistical moments considered.

As noted above, our findings are associated with the particularly challenging scenario of flow driven by a pumping well, where grid refinement requirements are driven by the feedback between the geostatistical parameters of the randomly heterogeneous *Y* field and the degree of non-uniformity of the flow field. These results are associated with a strongly non-uniform flow condition and domain sizes (relative to the conductivity correlation length) which enable exploring the region of the domain where statistical moments of hydraulic head and fluxes are mostly affected by the action of the pumping well (see the analytical solution of Riva et al., 2001). In this context, our findings can be considered as a basis upon which one can build future studies to ascertain the effect of conditioning (e.g., on available conductivity information) on the requirements associated with numerical grids employed for the solution of groundwater flow MEs under general (non-uniform) conditions.

Acknowledgments

This work was supported by National Nature Science Foundation of China (Grant No. J216065). Part of the work was developed while Prof. A. Guadagnini was at the University of Strasbourg with funding from Région Grand-Est and Strasbourg-Eurométropole through the 'Chair Gutenberg'.

References

Bianchi Janetti E, Riva M, Straface S, Guadagnini A (2010) Stochastic characterization of the Montaldo Uffugo research site (Italy) by geostatistical inversion of moment equations of groundwater flow. Journal of Hydrology 381: 42-51.

Geuzaine C, Remacle JF (2009) Gmsh: a three-dimensional finite element mesh generator with built-in pre- and post-processing facilities. Int J Numer Meth Eng 79(11): 1309-1331.

Guadagnini A, Neuman SP (1999a) Nonlocal and localized analyses of conditional mean steady state flow in bounded, randomly nonuniform domains: 1. theory and computational approach. Water Resour Res 35(10): 2999-3018.

Guadagnini A, Neuman SP (1999b) Nonlocal and localized analyses of conditional mean steady state flow in bounded, randomly nonuniform domains: 2. computational examples. Water Resour Res 35(10): 3019-3039.

Graf T, Degener L (2011) Grid convergence of variable-density flow simulations in discretely-fractured porous media. Adv Water Resour 34(6): 760-769.

Hernandez AF, Neuman SP, Guadagnini A, Carrera J (2003) Conditioning mean steady state flow on hydraulic head and conductivity through geostatistical inversion. Stoch Environ Res Risk Assess, 17: 329-338, https://doi.org/10.1007/s00477-003-0154-4.

Hristopulos DT (2006) Approximate methods for explicit calculations of non-Gaussian moments. Stoch Environ Res Risk Assess, 20: 278-290, https://doi.org/10.1007/s00477-005-0023-4.

Hu BX, Wu J, Zhang D (2004) A numerical method of moments for solute transport in physically and chemically nonstationary formations: linear equilibrium sorption with random K-d. Stoch Environ Res Risk Assess, 18: 22-30, https://doi.org/10.1007/s00477-003-0161-5.

Leube PC, De Barros FPJ, Nowak W, Rajagopal R (2013) Towards optimal allocation of computer resources: trade-offs between uncertainty quantification, discretization and model reduction. Environ Modell Softw 50(50): 97-107.

Li L, Tchelepi H, (2003) Conditional stochastic moment equations for uncertainty analysis of flow in heterogeneous reservoirs. SPE J 8(4): 393-400.

Li L, Tchelepi H, Zhang D (2003) Perturbation-based moment equation approach for flow in heterogeneous porous media: applicability range and analysis of high-order terms. J Comput Phys 188 (1): 296-317.

Li L, Tchelepi H, (2004) Statistical Moment Equations for Flow in Composite Heterogeneous Porous Media. ECMOR IX-9th European Conference on the Mathematics of Oil Recovery, Cannes, France, 30 August - 2 September.

Li L, Tchelepi H (2006) Conditional statistical moment equations for dynamic data integration in heterogeneous reservoirs. SPE J 9(3): 280-288.

Maina FH, Ackerer P, Younes A, Guadagnini A, Berkowitz B (2018) Benchmarking numerical codes for tracer transport with the aid of laboratory-scale experiments in 2D heterogeneous porous media. J Contam Hydrol 212: 55-64.

Neuman, S P, Guadagnini A, Riva M (2004) Type-curve estimation of statistical heterogeneity, Water Resour Res 40, W04201.

Neuman SP, Blattstein A, Riva M, Tartakovsky DM, Guadagnini A, Ptak T (2007) Type curve interpretation of late-time pumping test data in randomly heterogeneous aquifers. Water Resour Res 43(10): 2457-2463.

Panzeri M, Riva M, Guadagnini A, Neuman SP (2014) Comparison of ensemble Kalman filter groundwater-data assimilation methods based on stochastic moment equations and Monte Carlo simulation. Adv Water Resour 66(2): 8-18.

Panzeri M, Riva M, Guadagnini A, Neuman SP (2015) EnKF coupled with groundwater flow moment equations applied to Lauswiesen aquifer, Germany. J Hydrol 521: 205-216.

Richardson LF (1910) The Approximate Arithmetical Solution by Finite Differences of Physical Problems Involving Differential Equations, with an Application to the Stresses in a Masonry Dam, Lond Roy Soc Proc (A) 210: 307-357.

Richardson LF, Gaunt JA (1927) The deferred approach to the limit. Part I. Single lattice. Part II. Interpenetrating lattices. Philos Tr R Soc S-A 226: 299-361.

Riva M, Guadagnini A, Neuman SP, Franzetti S (2001) Radial flow in a bounded randomly heterogeneous aquifer. Transport Porous Med 45(1): 139-193.

Riva M, Guadagnini A, Bodin J, Delay F (2009) Characterization of the Hydrogeological Experimental Site of Poitiers (France) by stochastic well testing analysis, J Hydrol 369 (1-2): 154-164.

Riva M, Guadagnini A, Neuman SP (2017) Theoretical analysis of non-Gaussian heterogeneity effects on subsurface flow and transport, *Water Resour. Res*., 53(4), 2298-3012, doi:10.1002/ 2016WR019353.

Roache PJ (1994) Perspective: A method for uniform reporting of grid refinement studies. J Fluid Eng-T ASME 116(3): 405-413.

Slough KJ, Sudicky EA, Forsyth PA (1999) Grid refinement for modeling multiphase flow in discretely fractured porous media. Adv Water Resour 23(3): 261-269.

Stern F, Wilson RV, Coleman HW, Paterson EG (2001) Comprehensive approach to verification and validation of CFD simulations part 1: Methodology and procedures. J Fluid Eng 123(4): 793-802.

Tartakovsky D, Neuman SP (1997) Transient flow in bounded randomly heterogeneous domains 1. Exact conditional moment equations and recursive approximations. Water Resour Res 34 (1): 1-12.

Vassberg JC, Jameson A (2010) In Pursuit of Grid Convergence for Two-Dimensional Euler Solutions, J Aircraft 47(4): 1152-1166.

Weatherill D, Graf T, Simmons CT, Cook PG, Therrien R, Reynolds DA (2008) Discretizing the fracture-matrix interface to simulate solute transport. Ground Water 46(4): 606-615.

Winter CL, Tartakovsky D, Guadagnini A (2003) Moment differential equations for flow in highly heterogeneous porous media. Surv Geophys 24: 81-106.

Ye M, Neuman SP, Guadagnini A, Tartakovsky DM (2004) Nonlocal and localized analyses of conditional mean transient flow in bounded, randomly heterogeneous porous media. Water Resour Res 40: W05104.

Zhang D (2002) Stochastic Methods for Flow in Porous Media: Copying with Uncertainties. Academic, San Diego.

Zhang D, Lu Z (2004) An efficient, high-order perturbation approach for flow in random porous media via Karhunen-Loeve and polynomial expansions. J Comput Phys 194: 773-794.

Tables

Table 1. Main characteristics of the 15 families of grids employed in the grid convergence study (here, $\zeta = \lambda / \Delta x$, λ and Δx respectively being the correlation scale of the log-conductivity field (see Eq. (26)) and the grid size; N is the total number of nodes associated with a given grid).

Grid family	Coarse grid set		Medium grid set		Fine grid set	
	ζ	N	ζ	N	ζ	N
1	4	85	8	137	16	1345
2	6	137	12	689	24	2375
3	8	297	16	1185	32	4737
4	10	449	20	1793	40	7169
5	12	645	24	2577	48	10305
6	14	849	28	3393	56	13569
7	16	1153	32	4609	64	18433
8	18	1389	36	5553	72	22209
9	20	1749	40	6993	80	27969
10	22	2085	44	8337	88	33345
11	24	2469	48	9873	96	39489
12	26	2885	52	11537	104	46145
13	28	3273	56	13089	112	52353
14	30	3881	60	15521	120	62081
15	32	4437	64	17745	128	70977

Table 2. Estimates of the convergence order (p) calculated through Eq. (21) on the basis of Fig. 7. Values of the determination coefficients (R^2) of the corresponding regressions are also listed.

Moments	$\langle h^{(0)} \rangle$	$\langle h^{(2)} \rangle$	$\sigma_h^{2(2)}$	$\sigma_{qrr}^{2(2)}$	$\sigma_{q\theta\theta}^{2(2)}$	$C_h^{(2)}(\xi, \xi_1')$	$C_h^{(2)}(\xi, \xi_2')$	$C_h^{(2)}(\xi, \xi_3')$	$C_h^{(2)}(\theta, \xi_1')$	$C_h^{(2)}(\theta, \xi_2')$	$C_h^{(2)}(\theta, \xi_3')$
p	1.21	1.23	1.07	0.49	1.13	1.08	1.04	1.03	2.23	2.18	2.00
R^2	0.93	0.93	0.85	0.89	0.91	0.82	0.81	0.81	0.96	0.98	0.98

Figures

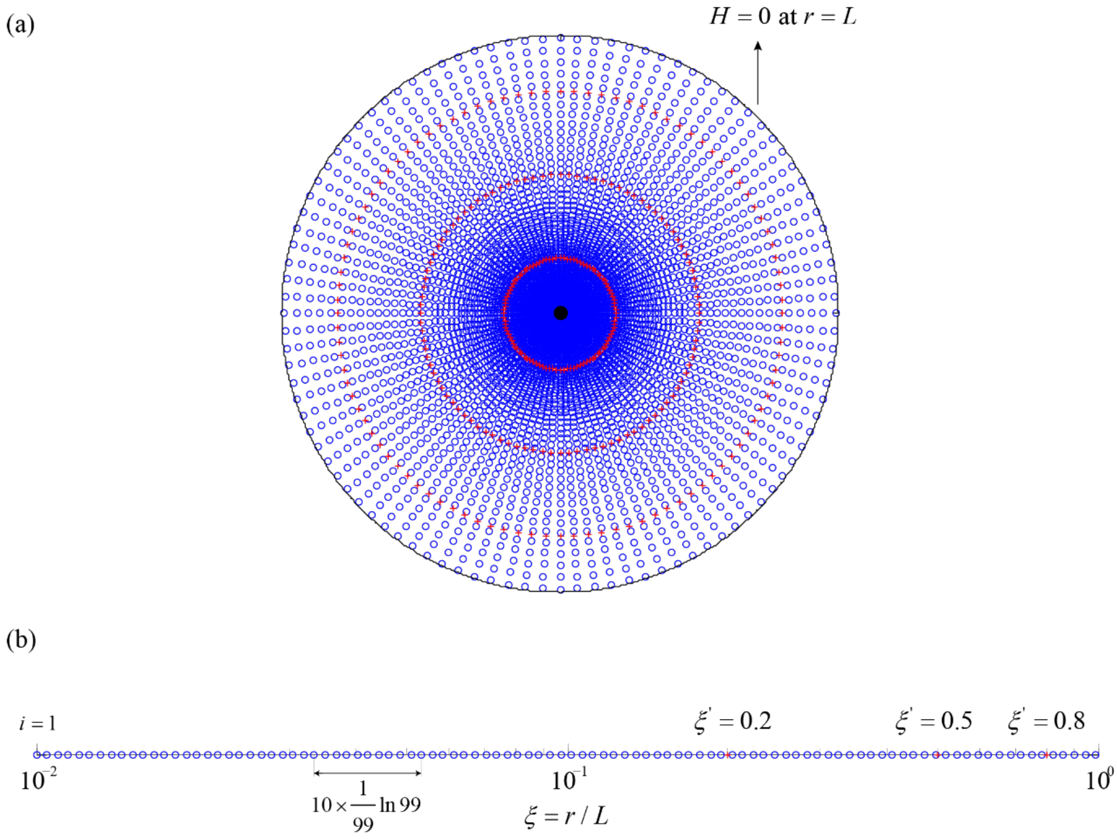

Figure 1. Flow domain and (a) spatial distribution of the reference points (o, +), and (b) detailed locations of the 100 reference points (o) in log scale along a generic radius for the comparisons between analytical and numerical solutions of the MEs. The pumping well (●) is located at the domain center.

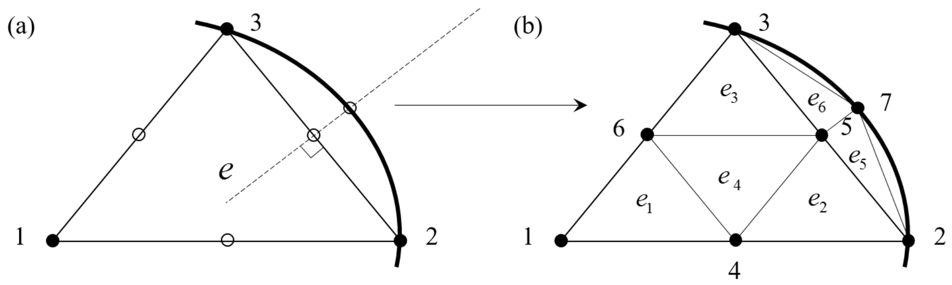

Figure 2. Details of the grid refinement at the domain boundary: (a) element e is divided into (b) 4 sub-elements (e_l; l = 1, 2, 3, 4) and two additional elements are generated, i.e., e_5 and e_6). The additional node (denoted as 7) is located on the domain boundary at equal distance from nodes 2 and 3.

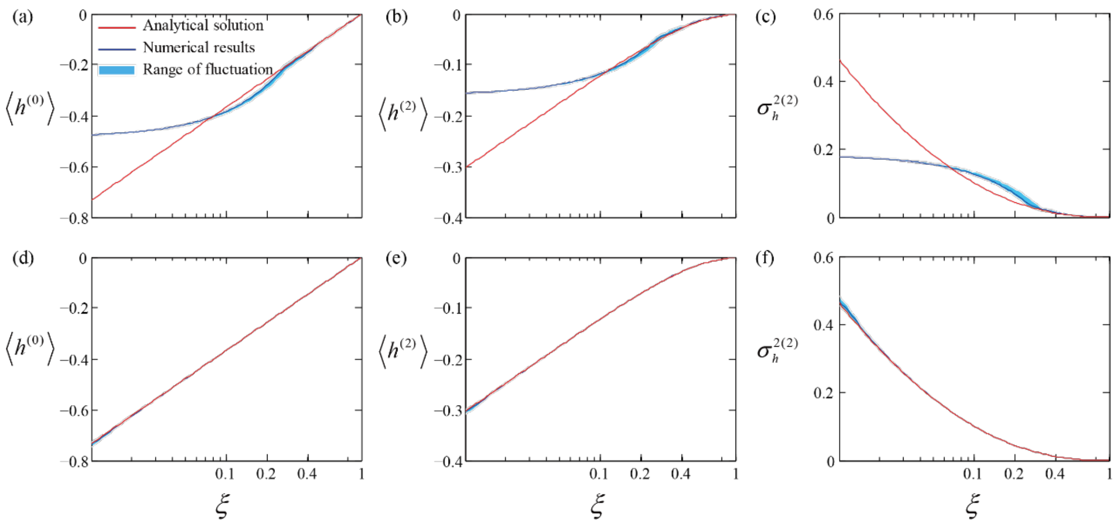

Figure 3. Numerical and analytical solutions for the zero- ($\langle h^{(0)} \rangle$) and second- ($\langle h^{(2)} \rangle$) order mean heads, together with second-order head variance ($\sigma_h^{2(2)}$) for (a, b, c) $TC_{1,c}$ and (d, e, f) $TC_{15,f}$. The dark blue solid curve represents the mean of the N_θ numerical values calculated for a given radial coordinate, the light blue band describing the range of fluctuation of the solutions; the red solid curve represents the corresponding analytical solution. Results are depicted for $L / \lambda = 1$, $\sigma_Y^2 = 1$, and $K_G = 1$.

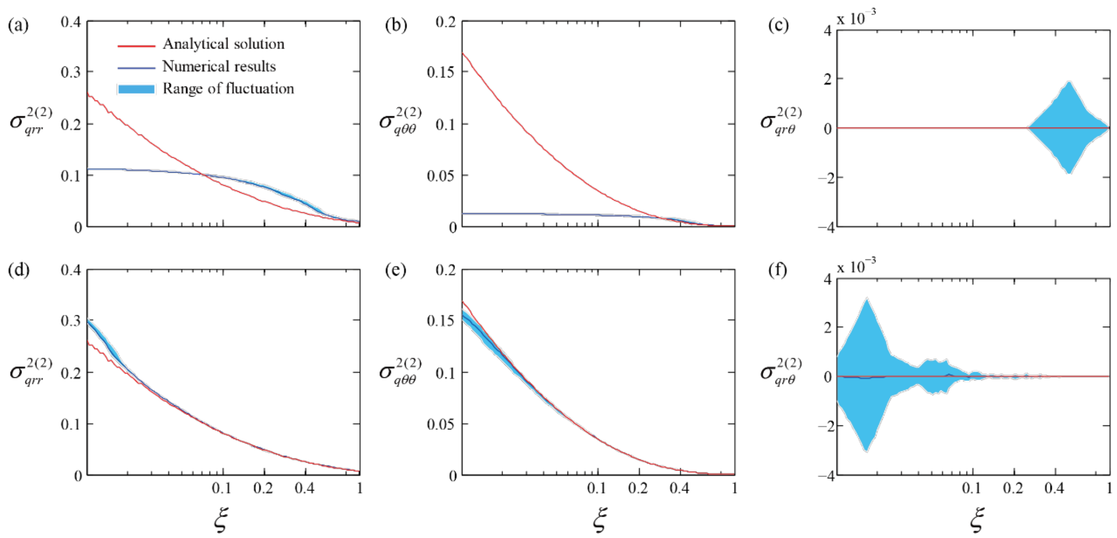

Figure 4. Numerical and analytical solutions of (second-order) flux variances $\sigma_{qrr}^{2(2)}$, $\sigma_{q\theta\theta}^{2(2)}$ and $\sigma_{qr\theta}^{2(2)}$ for (a, b, c) $TC_{1,c}$ and (d, e, f) $TC_{15,f}$. The dark blue solid curve represents the mean of the N_θ numerical values calculated for a given radial coordinate, the light blue band describing the range of fluctuation of the solutions; the red solid curve represents the corresponding analytical solution. Results are depicted for $L/\lambda = 1$, $\sigma_Y^2 = 1$, and $K_G = 1$.

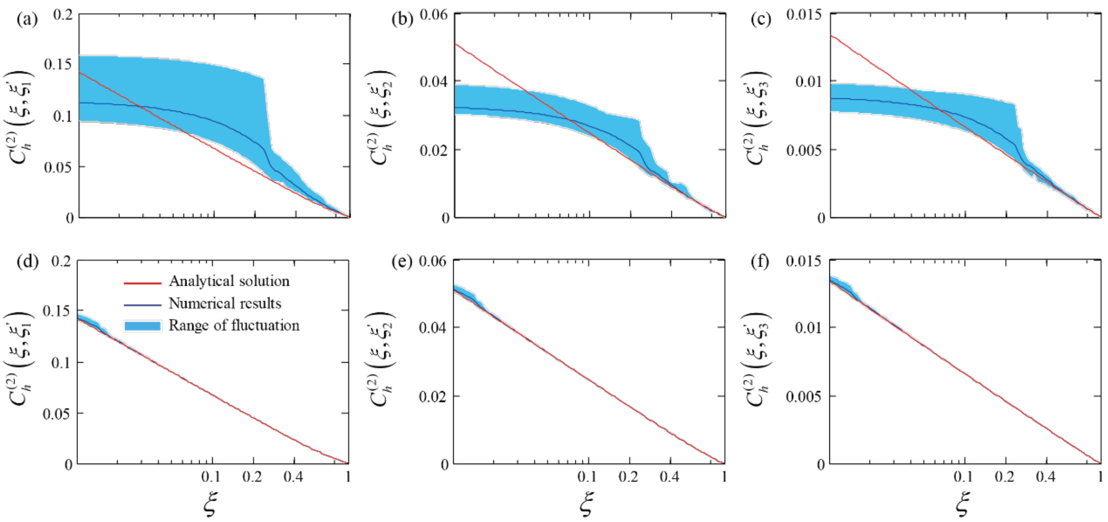

Figure 5. Numerical and analytical solutions of head covariances $C_h^{(2)}\left(\xi, \xi_1^{'}\right)$, $C_h^{(2)}\left(\xi, \xi_2^{'}\right)$, and $C_h^{(2)}\left(\xi, \xi_3^{'}\right)$ for (a, b, c) $TC_{1,c}$ and (d, e, f) $TC_{15,f}$. The dark blue solid curve represents the mean of the N_θ numerical values calculated for a given radial coordinate, the light blue band describing the range of fluctuation of the solutions; the red solid curve represents the corresponding analytical solution. Results are depicted for $L / \lambda = 1$, $\sigma_Y^2 = 1$, and $K_G = 1$.

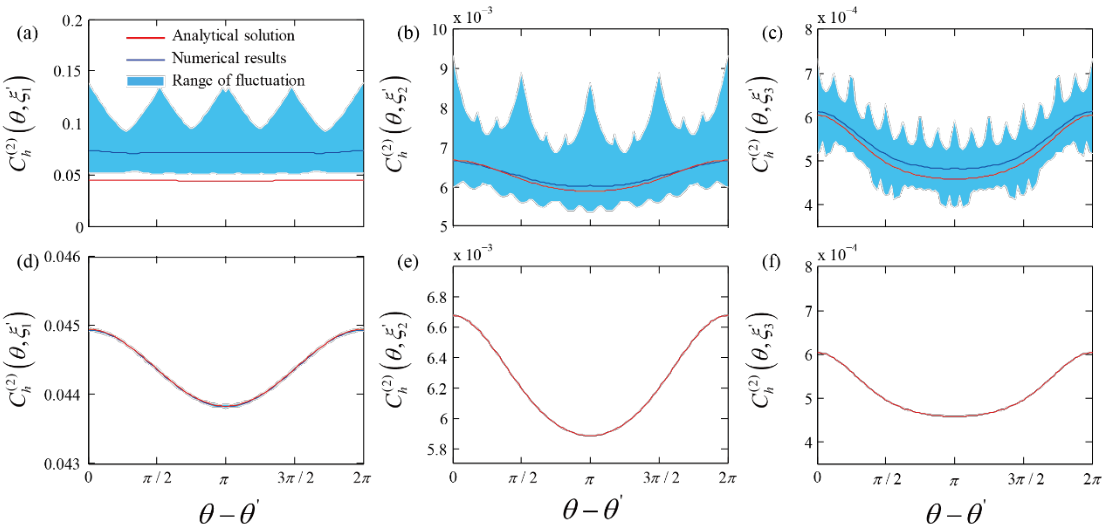

Figure 6. Numerical and analytical solutions of the head covariance $C_h^{(2)}\left(\theta, \xi_1'\right)$, $C_h^{(2)}\left(\theta, \xi_2'\right)$ and $C_h^{(2)}\left(\theta, \xi_3'\right)$ for (a, b, c) $TC_{1,c}$ and (d, e, f) $TC_{15,f}$. The dark blue solid curve represents the mean of the N_θ numerical values calculated for a given radial coordinate, the light blue band describing the range of fluctuation of the solutions; the red solid curve represents the corresponding analytical solution. Results are depicted for $L/\lambda = 1$, $\sigma_Y^2 = 1$, and $K_G = 1$.

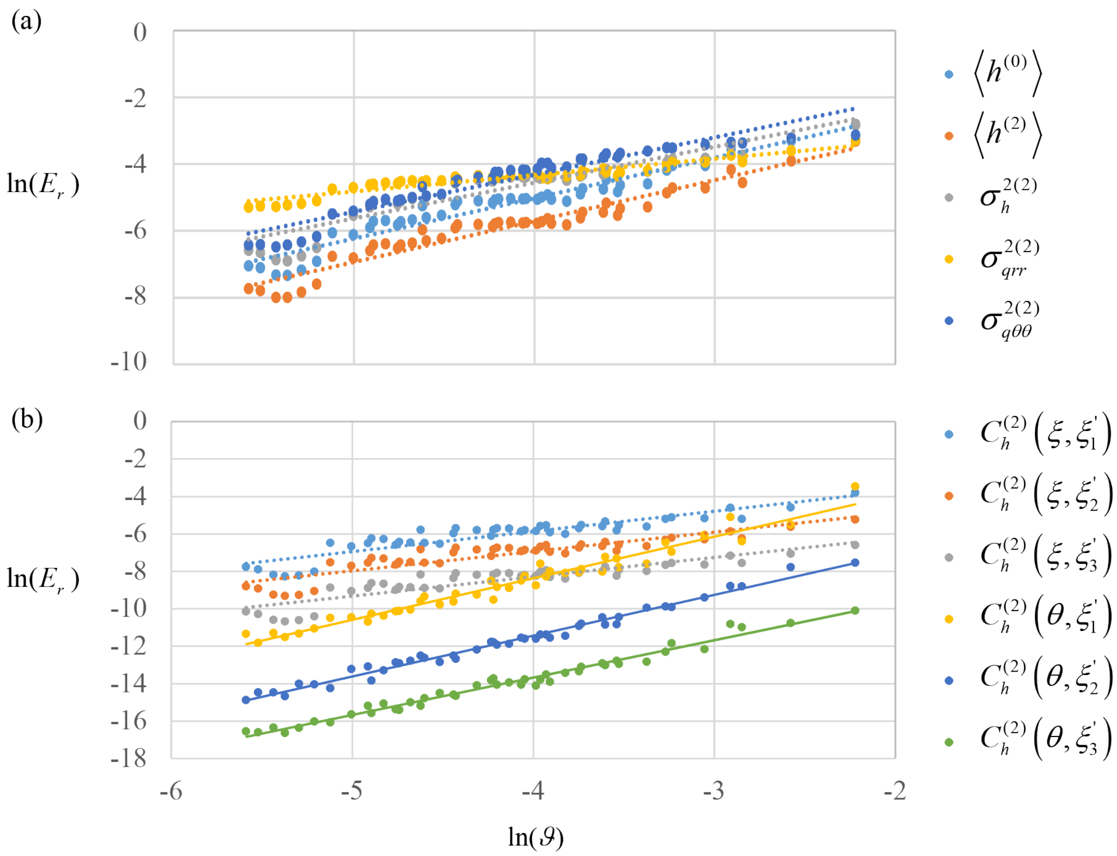

Figure 7. Values of $\ln E_r$ (28) versus $\ln(\vartheta) = -0.5\ln(N)$ for (a) $\langle h^{(0)} \rangle$, $\langle h^{(2)} \rangle$, $\sigma_h^{2(2)}$, $\sigma_{qrr}^{2(2)}$, and $\sigma_{q\theta\theta}^{2(2)}$; and (b) $C_h^{(2)}(\xi,\xi_1')$, $C_h^{(2)}(\xi,\xi_2')$ and $C_h^{(2)}(\xi,\xi_3')$ $C_h^{(2)}(\theta,\xi_1')$, $C_h^{(2)}(\theta,\xi_2')$ and $C_h^{(2)}(\theta,\xi_3')$. Straight (solid or dashed) lines are the results of (least square) linear regressions on numerical results. Results are depicted for $L/\lambda = 1$, $\sigma_Y^2 = 1$, and $K_G = 1$.

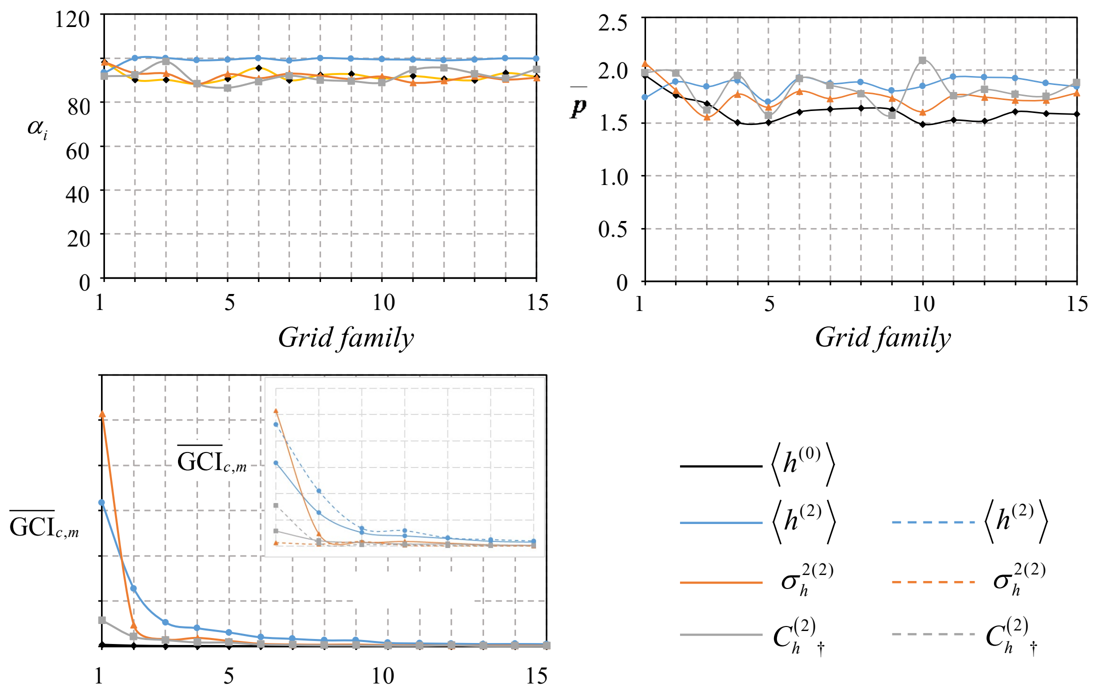

Figure 8. Values of (a) α_i (29); (b) $\bar{p}$ (i.e., averages of the corresponding values of p calculated via Eq. (23)) at the fraction of nodes depicted in (a); and (c) average $\mathrm{GCI}_{c,m}$ (25), denoted as $\overline{\mathrm{GCI}}_{c,m}$, versus grid family identifier (see Table 1). Results are depicted for $\langle h^{(2)} \rangle$, $\langle h^{(0)} \rangle$, $\sigma_h^{2(2)}$ and $C_{h\dagger}^{(2)}$ (i.e., the head covariance for the reference point $(\xi,\ \theta) \equiv (0.5,\ 0)$). Results are depicted for $L / \lambda = 1,\ 3$, $\sigma_Y^2 = 1$, and $K_G = 1$.

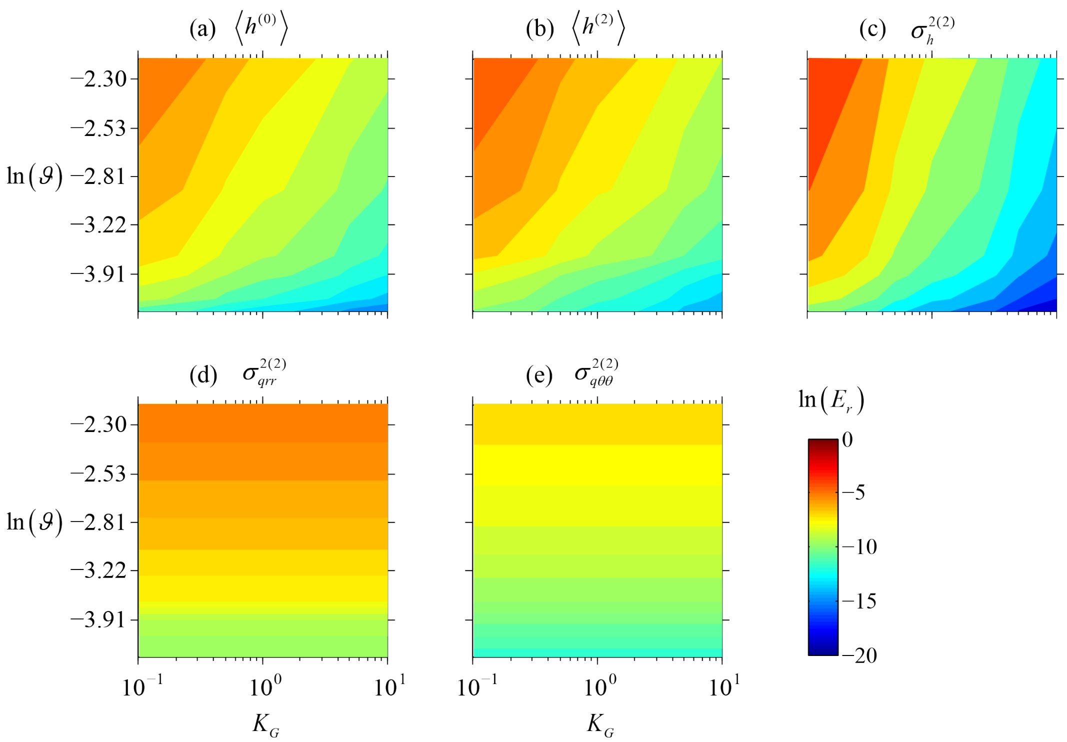

Figure 9. Dependence of E_r (28) on $K_G = e^{\langle Y \rangle}$ and ϑ for mean and variance of heads and variance of fluxes. Results are depicted for $L / \lambda = 1$, and $\sigma_Y^2 = 1$.

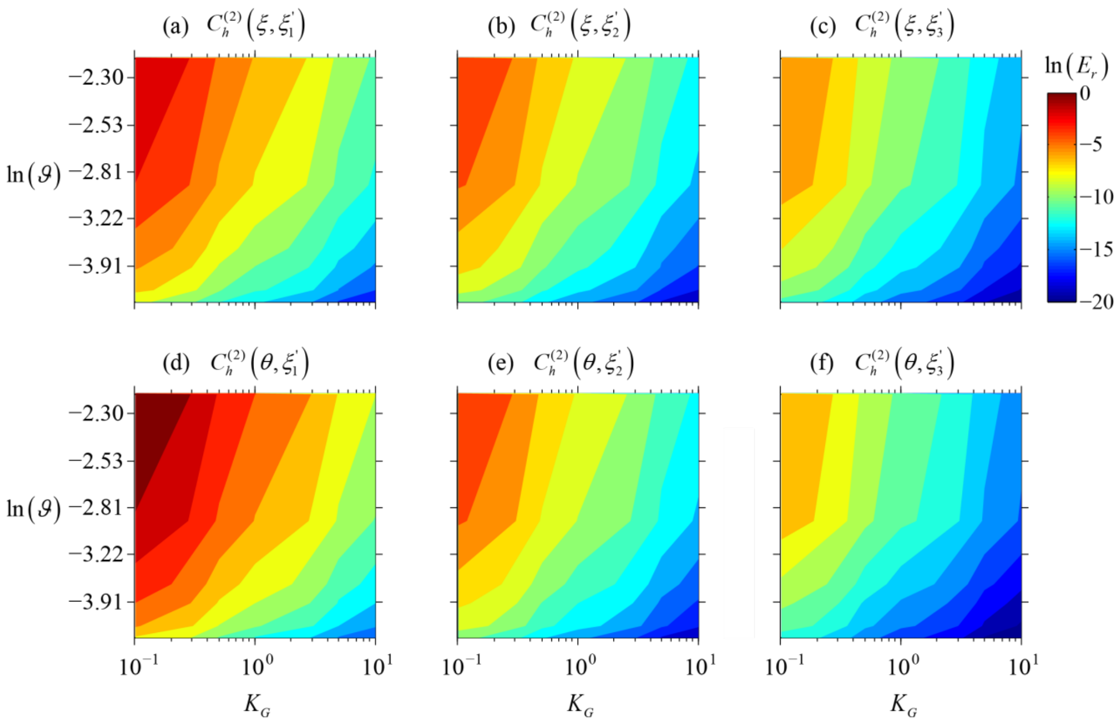

Figure 10. Dependence of E_r (28) on $K_G = e^{\langle Y \rangle}$ and ϑ for (a) $C_h^{(2)}(\xi,\xi_1')$, (b) $C_h^{(2)}(\xi,\xi_2')$, (c) $C_h^{(2)}(\xi,\xi_3')$, (d) $C_h^{(2)}(\theta,\xi_1')$, (e) $C_h^{(2)}(\theta,\xi_2')$, and (f) $C_h^{(2)}(\theta,\xi_3')$. Results are depicted for $L/\lambda = 1$, and $\sigma_Y^2 = 1$.

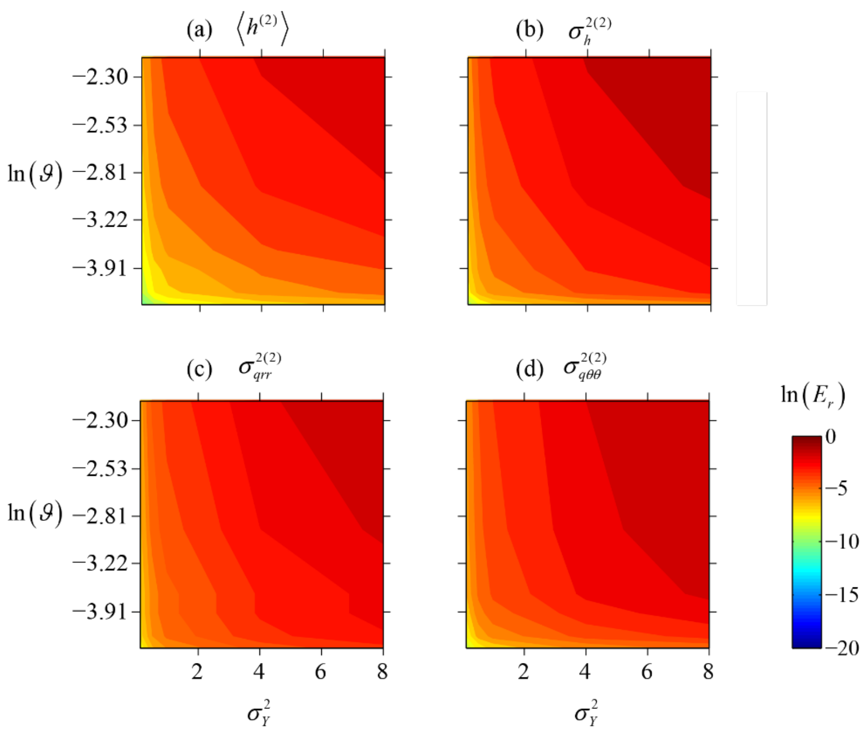

Figure 11. Dependence of E_r (28) on σ_Y^2 and ϑ for mean and variance of heads and variance of fluxes. Results are depicted for $L / \lambda = 1$, and $K_G = 1$.

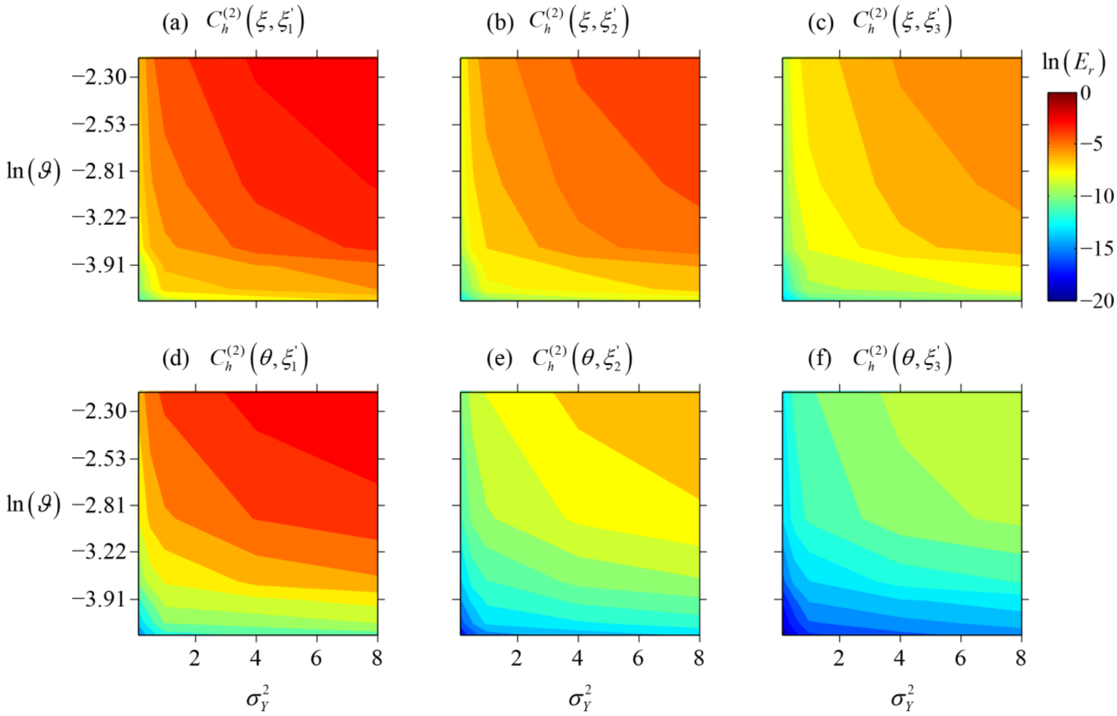

Figure 12. Dependence of E_r (28) on σ_Y^2 and ϑ for (a) $C_h^{(2)}(\xi,\xi_1')$, (b) $C_h^{(2)}(\xi,\xi_2')$, (c) $C_h^{(2)}(\xi,\xi_3')$, (d) $C_h^{(2)}(\theta,\xi_1')$, (e) $C_h^{(2)}(\theta,\xi_2')$, and (f) $C_h^{(2)}(\theta,\xi_3')$. Results are depicted for $L/\lambda = 1$, and $K_G = 1$.